AGU PUBLICATIONS

JGR

Journal of Geophysical Research: Atmospheres

RESEARCH ARTICLE
10.1002/2015JD023287

Key Points:
- Saharan mineral dust (MD) strongly alters snow radiative properties in the Alps
- Novel Snow Darkening Index (SDI) allows to represent the impact of MD on snow
- Differences between observed and simulated spectra were ascribed to large particles (>30 μm)

Correspondence to:
B. Di Mauro,
b.dimauro@campus.unimib.it

Citation:
Di Mauro, B., F. Fava, L. Ferrero, R. Garzonio, G. Baccolo, B. Delmonte, and R. Colombo (2015), Mineral dust impact on snow radiative properties in the European Alps combining ground, UAV, and satellite observations, *J. Geophys. Res. Atmos.*, *120*, 6080–6097, doi:10.1002/2015JD023287.

Received 19 FEB 2015
Accepted 25 MAY 2015
Accepted article online 28 MAY 2015
Published online 21 JUN 2015

Mineral dust impact on snow radiative properties in the European Alps combining ground, UAV, and satellite observations

B. Di Mauro[1], F. Fava[1], L. Ferrero[2], R. Garzonio[1], G. Baccolo[3,4,5], B. Delmonte[3], and R. Colombo[1]

[1]Remote Sensing of Environmental Dynamics Laboratory, Department of Earth and Environmental Sciences, University of Milano-Bicocca, Milan, Italy, [2]POLARIS Research Center, Department of Earth and Environmental Sciences, University of Milano-Bicocca, Milan, Italy, [3]Department of Earth and Environmental Sciences, University of Milano-Bicocca, Milan, Italy, [4]National Institute of Nuclear Physics (INFN), Section of Milano-Bicocca, Milan, Italy, [5]Earth Sciences Department, University of Siena, Siena, Italy

Abstract In this paper, we evaluate the impact of mineral dust (MD) on snow radiative properties in the European Alps at ground, aerial, and satellite scale. A field survey was conducted to acquire snow spectral reflectance measurements with an Analytical Spectral Device (ASD) Field Spec Pro spectroradiometer. Surface snow samples were analyzed to determine the concentration and size distribution of MD in each sample. An overflight of a four-rotor Unmanned Aerial Vehicle (UAV) equipped with an RGB digital camera sensor was carried out during the field operations. Finally, Landsat 8 Operational Land Imager (OLI) data covering the central European Alps were analyzed. Observed reflectance evidenced that MD strongly reduced the spectral reflectance of snow, in particular, from 350 to 600 nm. Reflectance was compared with that simulated by parameterizing the Snow, Ice, and Aerosol Radiation radiative transfer model. We defined a novel spectral index, the Snow Darkening Index (SDI), that combines different wavelengths showing nonlinear correlation with measured MD concentrations ($R^2 = 0.87$, root-mean-square error = 0.037). We also estimated a positive instantaneous radiative forcing that reaches values up to 153 W/m^2 for the most concentrated sampling area. SDI maps at local scale were produced using the UAV data, while regional SDI maps were generated with OLI data. These maps show the spatial distribution of MD in snow after a natural deposition from the Saharan desert. Such postdepositional experimental data are fundamental for validating radiative transfer models and global climate models that simulate the impact of MD on snow radiative properties.

1. Introduction

The cryosphere is an integral part of the Earth system that includes the highest reflecting natural surfaces (albedo greater than 0.95 in visible spectrum for pristine snow). The cryosphere plays a significant role in the global climate system and is particularly sensitive to very small variations in the amount of reflected/absorbed radiation, which have shown to produce significant effects on the hydrological cycle and the energy balance of the Earth system at different spatial scales [*Flanner and Zender*, 2005; *Flanner et al.*, 2007; *Bond et al.*, 2013; *Painter et al.*, 2013a]. Besides the widespread general reduction in snow cover extent, changes in the cryosphere associated with a general decrease in surface snow albedo are also involved in the positive feedback of a warming climate and represent a topic of great societal concern.

Light absorption due to impurity content in snow and ice is involved in complex mechanisms such as the snow albedo positive feedback [*Hansen and Nazarenko*, 2004; *Myhre et al.*, 2013], which represents a classical example of nonlinearity in the climate system, that is, the more the snow melts, the more radiation is absorbed and the more other snow melts. This process has shown to produce a significant impact on snow chemical [*Rhoades et al.*, 2010] and radiative properties [*Clarke and Noone*, 1985; *Flanner et al.*, 2007, 2009], snow hydrology [*Hadley et al.*, 2010; *Painter et al.*, 2012a; *Sterle et al.*, 2013; *Kaspari et al.*, 2015], timing of snowmelt [*Li et al.*, 2013], vegetation phenology [*Steltzer et al.*, 2009], and also glacier retreat [*Oerlemans et al.*, 2009; *Wientjes et al.*, 2011; *Painter et al.*, 2013a].

The optical properties of snow and ice depend largely on the shape and dimension of their crystals: with an increase in the size of the crystals (often referred as grain size or "effective radius," according to Mie's theory

[*Mie*, 1908; *Wiscombe*, 1980]), reflected radiance decreases with great sensitivity at near-infrared and longer wavelengths [*Wiscombe and Warren*, 1980; *Warren*, 1982]. Light-absorbing impurities can also influence snow optical properties. Typical impurities are represented by carbonaceous particles [*Flanner et al.*, 2007; *Hadley and Kirchstetter*, 2012; *Doherty et al.*, 2014; *Meinander et al.*, 2014], volcanic ash [*Conway et al.*, 1996], and mineral dust [*Painter et al.*, 2010, 2012a, 2013b; *Li et al.*, 2013]. When deposited in snow, this particulate matter acts, at different degrees, like a blackbody absorbing radiation and thermalizing it through the media. This process alters the radiative balance of snow and ice, causing the absorption of an additional amount of radiation (i.e., radiative forcing, RF) and ultimately influencing surface melting processes of snow and ice.

Some methods based on numerical modeling have been proposed in literature with the aim of estimating the RF due to light-absorbing impurities such as black carbon (BC), mineral dust (MD), and volcanic ash deposited on snow and ice [*Jacobson*, 2004; *Flanner et al.*, 2007; *Aoki et al.*, 2011; *Yasunari et al.*, 2011; *Bauer and Ganopolski*, 2014]. While BC is emitted from both natural (e.g., forest fires) and anthropogenic (*e.g.,* fossil fuel and biofuel combustion) sources [*Bond et al.*, 2013], the main sources of MD are represented by arid regions with low vegetation cover where fine-grained material is available [*Prospero*, 2002]. Once suspended in the atmosphere, MD aerosol influences climate both directly and indirectly [*Goudie and Middleton*, 2001; *Claquin et al.*, 2003; *Field et al.*, 2010; *Mahowald et al.*, 2013]. The direct effect consists mainly of changing the radiative properties of the atmosphere through the scattering and absorption of solar and terrestrial radiation. Conversely, the indirect effect of MD consists of acting as cloud condensation and ice nuclei and modifying cloud properties by delivering micronutrients (e.g., Fe) to the ocean [*Mahowald et al.*, 2005; *Winton et al.*, 2014] and modulating the uptake of carbon in the marine ecosystems and the atmospheric concentration of CO_2 [e.g., *Maher et al.*, 2010, and references therein]. On the other hand, production and transport of dust are itself extremely sensitive to climate change and are a current topic of active research; in this respect, past atmospheric conditions and particle deposition in mountainous and nonmountainous areas over the last centuries are widely studied using ice cores from nonpolar glaciers and ice caps [*Sodemann et al.*, 2006; *Thevenon et al.*, 2009] and land-atmosphere model simulations [*Lawrence et al.*, 2011; *Albani et al.*, 2014].

Today, much scientific literature exists on numerical modeling [*Jacobson*, 2004; *Flanner et al.*, 2007; *Aoki et al.*, 2011; *Yasunari et al.*, 2011, 2015; *Liou et al.*, 2014] and controlled experiments on light-absorbing impurities on snow [*Brandt et al.*, 2011; *Hadley and Kirchstetter*, 2012; *Meinander et al.*, 2014]. However, only a few studies present field spectral data collected after events of MD deposition on snow and they are mainly located in the United States and Asia. These studies are fundamental for understanding the actual radiative effect of MD in snow-covered areas [*Pedersen et al.*, 2015] and for validation of radiative transfer (RT) models such as the Snow, Ice, and Aerosol Radiation (SNICAR) model [*Flanner et al.*, 2007, 2009]), which is included in the Community Land Model [*Lawrence et al.*, 2011]. In fact, those models are widely applied for local and global prediction of light-absorbing impurities in snow and ice [*McConnell et al.*, 2007; *Hadley and Kirchstetter*, 2012; *Lin et al.*, 2014].

Despite some uncertainties for BC [*Warren*, 2013], MD deposition on snow has been successfully investigated in the recent past using remotely sensed data [*Painter et al.*, 2012b, 2013b; *Gautam et al.*, 2013; *Li et al.*, 2013; *Dumont et al.*, 2014]. Recent studies have analyzed the impact of MD on snow and ice by integrating ground and satellite observations to physically based models. These researches suggest that MD depositions alter the radiative balance of the region considered owing to the reduction of the snow cover associated with an increased melting rate that exposes darker surfaces (e.g., soil or vegetation) to direct solar radiation.

Some of these studies have also been conducted on the MD impact on snow in the Colorado river basin [*Painter et al.*, 2012a; *Bryant et al.*, 2013], Himalayan chain [*Painter et al.*, 2012b; *Gautam et al.*, 2013], Greenland [*Carmagnola et al.*, 2013; *Dumont et al.*, 2014], Iceland [*Dagsson-Waldhauserova et al.*, 2015], and Caucasus mountains [*Kutuzov et al.*, 2013], also in relation to the mineralogical composition of MD [*Reynolds et al.*, 2013].

Despite this increasing interest in the MD impact on snow, to date, no studies that evaluate the BC and MD impact on snow have been conducted in the European Alps. The European Alps are considered to be highly sensitive to climatic and environmental conditions, and even slight changes in radiative balances in mountain areas can influence the hydrological cycle and glacier retreat. These dependencies were also

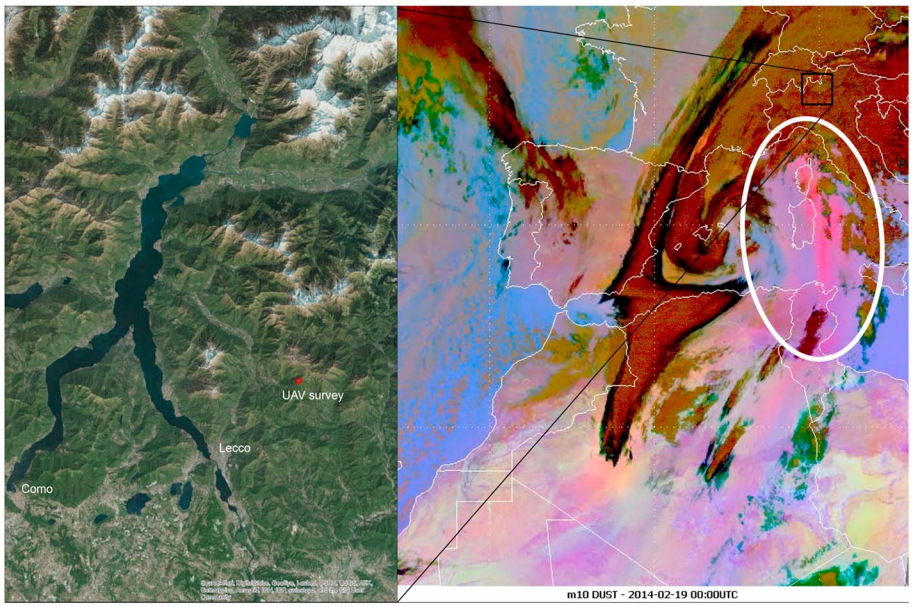

Figure 1. (left) Focus on the central European Alps. The red polygon represents the test site on the Artavaggio plains, where the UAV survey was performed. (right) Aeolian transport of MD from the Sahara desert (white ellipse) as seen by the MSG-SEVIRI Dust RGB product (copyright 2014 EUMETSAT). Dust RGB product represents dust in pink/magenta, instead clouds are represented in brown/orange. Further information about the dust transport event can be found at http://www.eumetsat.int/website/home/Images/ImageLibrary/DAT_2104098.html.

highlighted in a recent study, suggesting that the deposition of industrial BC on snow may have played an important role in forcing the end of the Little Ice Age in the Alps [*Painter et al.*, 2013a]. The importance of MD on the Alps is stressed by the fact that a large amount of MD can be transported long range from North Africa to Europe [*Tschiersch et al.*, 1990; *Sodemann et al.*, 2006], with significant direct and indirect radiative effects [*Helmert et al.*, 2007]. During these events, aeolian MD can also reach areas covered by seasonal or perennial snow and ice in the Alps [*De Angelis and Gaudichet*, 1991; *Franzén et al.*, 1995].

In this context, we have tried to fill the aforementioned gaps by measuring snow optical properties and MD content of a seasonal snowpack using a multiscale approach in a test site in the European Alps, a few days after a significant MD transport event occurred in February 2014.

The main objective of this study is to investigate how Saharan MD alters Alpine snow optical properties by exploiting a combined approach based on ground hyperspectral measurements, a survey of an Unmanned Aerial Vehicle (UAV) and Landsat 8 Operational Land Imager (OLI) satellite data. Specific objectives of this study are as follows:

1. to compare experimental data with a physically based radiative transfer (RT) model;
2. to develop a novel spectral index sensitive to MD concentration in snow; and
3. to exploit a spectral index to represent the spatial patterns of MD deposition on snow.

2. Study Area and Mineral Dust Transport

The campaign was conducted after a significant transport of MD from the Saharan desert occurred in February 2014. In the Mediterranean area, under peculiar meteorological conditions [*Pey et al.*, 2013], such as the passage of a cold front over the source and low pressure patterns over the Mediterranean Sea causing Sirocco (from southeast) or Libeccio winds (from southwest), dust can be suspended in the atmosphere and transported for hundreds of kilometers. These atmospheric conditions are quite frequent in the spring season in the Northern Hemisphere, and they are mainly dictated by meteo-climatic patterns such as the North Atlantic Oscillation (NAO) [*Thevenon et al.*, 2009]. The study area is located on the Artavaggio plains (Lecco, Italy) at 1650 m above sea level near lake Lecco in a small portion of the central European Alps (Figure 1). MD was entrained in the troposphere over the North African Grand Erg Oriental

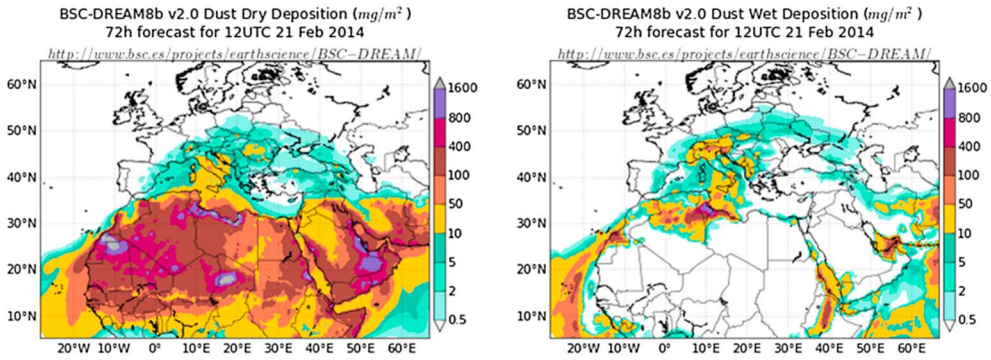

Figure 2. Dry and wet MD depositions as forecasted by the BSC-DREAM8 model. Image from the BSC-DREAM8b (Dust REgional Atmospheric Model) model, operated at the Barcelona Supercomputing Center (http://www.bsc.es/projects/earthscience/BSC-DREAM).

(Saharan lowlands of northeast Algeria) on 18 February during the passage of a cold front and then transported NE over the Mediterranean Sea by cyclonic atmospheric transport ("cutoff" block). Meteosat Second Generation–Spinning Enhanced Visible and Infrared Instrument (MSG-SEVIRI) data monitored the transport through the Dust RGB product (Figure 1) in which the brightness temperatures at different infrared channels are combined to enhance the presence of MD layers in the atmosphere. As the plume reached the Italian peninsula, it was deposited by both wet and dry depositions over the Alpine chain. These depositions were forecasted by the BSC-DREAM-8b model [*Basart et al.*, 2012] operated at the Barcelona Supercomputing Center (Figure 2). The model predicted a significant amount (~50–100 mg/m^2) of MD to be deposited on the European Alpine chain as wet deposition (rain and snow).

3. Materials and Methods

3.1. Field and Laboratory Measurements

A field measurement campaign was organized on the Artavaggio plains on 14 March 2014, a few weeks after the MD deposition at the site on 19 February. The date of the campaign was chosen after a visual inspection of the heterogeneous outcrop of the MD due to the melting of the snow with the arrival of the spring. This situation generated a unique condition of high spatial variability, which allowed observation of the radiative effect (e.g., albedo decrease) of MD deposition on Alpine seasonal snowpacks.

In total, 10 sampling areas (each of 2 m^2) were defined on the Artavaggio plains. Sampling areas were selected by visual inspection to have a significant variability of MD concentration among samples. Three snow sampling areas were selected as "blanks," while seven others were selected because of their MD content. In this sense, blanks represent the cleanest snow in the area, but they contain a certain amount of impurities (i.e., aerosol particles) of different natures. For each area, snow spectral reflectance was measured with a nonimaging hyperspectral radiometer, Analytical Spectral Devices (ASD) Field Spec pro. The instrument collects electromagnetic radiation ranging from 350 to 2500 nm with a full width at half maximum of 5–10 nm and a spectral resolution of 1 nm. The measured reflected radiance $L_{ref}(\lambda)$ was converted into reflectance units $\rho(\lambda)$ normalizing for incident radiance $L_{inc}(\lambda)$ collected using a calibrated Lambertian Spectralon® panel. Spectral data were collected at each sampling area in clear-sky conditions during ~3 h. Spectral measurements were performed using a bare optical fiber with a field of view of 25°. The distance between the optical fiber and the snow sample was 80 cm. The measurement was repeated 3 times for each area to calculate both the mean and the standard deviation of the reflectance.

Surface snow density and grain size were also measured in the field (first 5 cm of snow), this latter by comparison with a micron-sized grid.

Snow samples were collected from the first 5 cm of the snowpack using glass bottles of 1 L each. The bottles were previously cleaned 3 times with ultrapure water (Milli-Q®; 18.2 MΩ cm at 25°C; Water Purification System, Millipore, Bedford, MA, USA) exposing them for 20 min in an ultrasonic bath (SONICA®, Soltec, Italy).

Table 1. Concentration of MD for the Control (C1-3) and the Dust Sample (DS1-7) Determined With the Coulter Counter (CC) and the Gravimetric Method (GM)[a]

ID	C1	C2	C3	DS1	DS2	DS3	DS4	DS5	DS6	DS7
MD ppm (CC)	0.92	0.8	1.37	84.8	54.65	29	57.8	76.84	107.4	39.6
MD ppm (GM)	2.98	3.77	3.31	198.95	154.13	231.57	132.36	295.6	325.57	/

[a]Notice that sample 7 (DS7) was damaged during transportation to the laboratory.

After collection, the snow samples were stored in a polystyrene box surrounded by snow and transported to the University Campus in 2 h, where they were stored at −20°C in darkness until they were analyzed. Snow samples were analyzed in a cold room to determine mass concentration and size distribution of MD (section 3.2).

The concentration and size distribution of the insoluble particles were determined through two different methods: (1) a counting method (size range: 1–30 μm) and (2) a gravimetric method (total bulk concentration).

The choice of using two experimental methods for MD characterization depends on the possibility of taking advantage of the strengths of each experimental technique: (1) the counting method allowed experimental determination of the MD size distribution in input to the simulation of the reflectance spectra using the Snow, Ice, and Aerosol Radiation (SNICAR) model; and (2) the gravimetric method allowed experimental determination of the particulate matter mass concentration even below 1 μm and above 30 μm.

The counting method used a Coulter Counter (CC) technique. Samples were melted in a clean room (class 1000 clean room at EuroCold laboratory facilities, University of Milano-Bicocca) and diluted by a factor of ~10 with ultrapure (Milli-Q) water. Analyses were carried out using a Multisizer™ 3 COULTER COUNTER®, set to measure particles with a diameter (equivalent spherical) between 1 and 30 μm in 300 size channels. To obtain dust mass from particle volume, a typical crustal density of 2.5 g/cm^3 was adopted. MD total concentration from the CC method was estimated from the integral of the concentration between 1 and 18 μm to separate the contribution of MD particles from larger particles present in the sampled snow. Laboratory blanks were in all cases more than 100 times lower than the diluted samples. All steps of the analytical protocol followed *Delmonte et al.* [2002] and *Ruth et al.* [2008].

The gravimetric method (GM) allowed determination of the total mass concentration (ppm in melted snow) of MD deposited in the snow. Samples were first melted at ambient temperature (20°C) inside their own glass bottles used during the snow sampling, thus avoiding any external contamination during the melting. A magnetic stirred bar, precleaned with ultrapure water (Milli-Q), allowed homogenization of the sample using magnetic stirring. The volume of the melted samples was determined using a graduated cylinder with a precision of ±1 mL. The mass of the total particulate matter (PM: MD + other particles) in the melted snow was first collected using Millipore® filtering system equipped with a Whatman Quartz Fiber Filters (ø = 47 mm). The mass of the filtered PM was determined as the weight difference of the filters observed after and before filtration of the melted snow. The weight of the filters was determined as the average value of three weights measured both before and after filtration of the melted snow using a Sartorius® SE2-F microbalance with a precision of ±0.1 μg.

Before weighing, the filters were kept for 48 h at 20°C in darkness inside a silica gel dryer (RH < 2%) to remove all the water content. The final MD mass concentration was determined as the difference between the total PM concentration measured in each sample and the average PM concentration measured in the three blank samples. Considering the whole data set and each source of uncertainty, the average error associated with the MD mass concentration in the snow was ±0.87 ppm. As the MD concentration in the snow was very high (section 4.1 and Table 1), this uncertainty represents on average 0.42% of the measured MD and can be considered negligible for the scope of the present application.

3.2. Airborne and Satellite Data

During the field measurements, an Unmanned Aerial Vehicle (UAV) survey was performed to study the impact of MD on snow at local scale. A Landsat 8 tile was also collected to analyze the impact of MD at regional scale in the Alps. Data acquisition and processing scheme are described in the following sections.

3.2.1. Unmanned Aerial Vehicle (UAV) Survey

Recently, Unmanned Aerial Vehicles (UAVs) have been widely used for environmental monitoring [*Hodson et al.*, 2007; *Whitehead et al.*, 2013; *Immerzeel et al.*, 2014; *Lucieer et al.*, 2014], in particular, for surveys in snow- and ice-covered areas difficult to reach for ground observation [*Ryan et al.*, 2015]. In this work we used a four-rotor UAV (ANTEOS, produced by http://www.aermatica.com) equipped with an RGB digital camera (model: Canon s100) that is automatically triggered (1 image/s). The UAV is also equipped with a full inertial navigation system and with a Global Positioning System (GPS). The positioning data are used to precisely control the flight, to locate the UAV, and to tag all data collected from the sensors. The sensor data are continuously displayed over a mission map in the Ground Control Station (GCS) monitor. RGB images collected onboard are digitized and sent through the wireless link directly to the GCS, where the operator can view the images and telemetry data (GPS coordinates, flight altitude, flight speed, roll, pitch, and yaw) in the real-time mode. The UAV weighs 9 kg and is able to carry a maximum payload of 2 kg with a flight autonomy of 20 min. With blades unfolded, the UAV features a width of 200 cm, a length of 200 cm, and a height of 55 cm. Maximum forward flight speed is 5 m/s.

Two UAV overflights were organized to cover the whole study area. The altitude of the test site reduced the flight autonomy of the UAV, which flew at 30 m from the ground level for ~10 min/flight. RGB images acquired from the UAV survey (more than 600 images) were resampled to reduce computation time and then processed with a structure from motion (SFM) algorithm [*Westoby et al.*, 2012] implemented in the Agisoft Photoscan© package (http://www.agisoft.com/). SFM processing allows exploitation of the overlap between adjacent images and creation of georeferenced orthomosaic maps and high-resolution digital surface models (DSMs) of the test site. The position of the camera for each image was retrieved from the UAV telemetry acquired at constant frequency (1 data package/1 s).

3.2.2. Landsat OLI Data

A Landsat 8 Operational Land Imager (OLI) scene acquired the day before the campaign (13 February) was downloaded from the U.S. Geological Survey Global Visualization Viewer (http://glovis.usgs.gov) repository. The OLI sensor collects reflected radiance in nine spectral channels from visible to near-infrared wavelengths with a spatial resolution of 30 m [*Irons et al.*, 2012]. The nine OLI bands were converted first into top of atmosphere radiance and then into reflectance using the OLI calibration coefficients.

The correction for topographic and atmospheric effects of Landsat 8 OLI data was carried out using the ATCOR 3 code (Atmospheric/Topographic Correction for Mountainous Terrain) [*Richter*, 2007]. Similar to the whole ATCOR suite, ATCOR 3 also uses look-up tables generated by MODTRAN [*Berk et al.*, 1989], relating sensor radiances and albedo for various atmospheric and geometric conditions. Then ATCOR 3 includes the capability for radiometric correction in rugged terrain considering cast shadow and illumination calculations. In this study, ATCOR 3 was run with a winter midlatitude atmospheric profile and an image-based estimate of the visibility based on the dark dense vegetation approach [*Kaufman and Sendra*, 1988]. The Advanced Spaceborne Thermal Emission and Reflection (ASTER) global digital elevation model (GDEM) at 30 m spatial resolution was used for removing topographic effects. These corrections allowed removal of the atmospheric contribution by retrieving top of surface (TOS) reflectance and avoidance of the effect of shadow, which is substantial in areas with complex topography such as the Alps.

3.3. RT Modeling

Measured reflectances were compared to those simulated with the Snow, Ice, and Aerosol Radiation (SNICAR) model [*Flanner et al.*, 2007, 2009]. The model simulates hemispherical reflectance spectra between 300 and 5000 nm with a resolution of 10 nm. Model simulations were obtained by parameterizing the SNICAR radiative transfer model with observed variables. Those variables are snow grain size (μm), snow density (Kg/m^3), snowpack thickness (m), surface spectral distribution, solar zenith angle, and MD concentration in four particle dimension classes (0.1–1.0 μm, 1.0–2.5 μm, 2.5–5.0 μm, and 5.0–10.0 μm). The comparison between observed and simulated data was made to benchmark the model with direct reflectance measurements of snow containing a significant amount of light-absorbing impurities.

3.4. Spectral Index Development

Spectral data collected at different scales (field, UAV, and satellite) and modeled data were used to test the possibility of retrieving the presence of MD in snow. To achieve this goal, a set of linear and

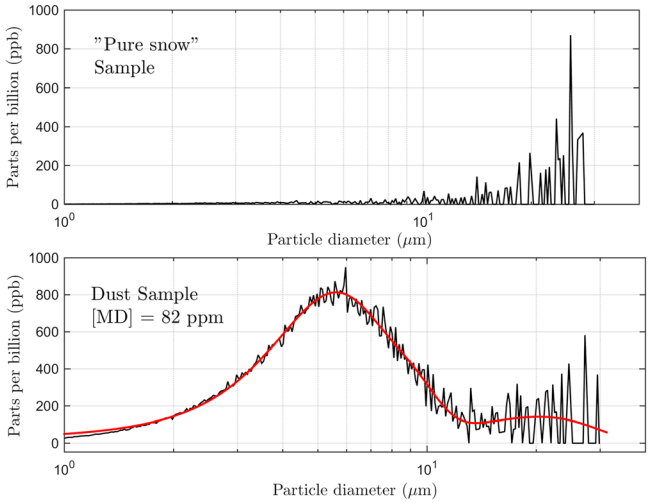

Figure 3. Size distribution of dust particles for a (top) control sample and a (bottom) snow sample containing 84 ppm of MD. The red line depicts a log-normal fit of the main distribution ($R^2 = 0.92$) (Note that the abscissa is represented in a logarithmic scale in both plots).

nonlinear ordinary least squares (OLS) regressions were performed between algebraic combinations of reflectance in specific wavelengths and MD concentration measured at each sampling area. The algebraic combination used for the spectral index is widely used to enhance differences in the reflectance of surfaces; it can be expressed in the form of a normalized ratio, as for example, the normalized difference snow index [*Hall et al.*, 1995], for snow classification.

The choice of the values of the two wavelengths was performed according to *Hansen and Schjoerring* [2003] and *Fava et al.* [2009], where all possible combinations of wavelengths are explored. Then the spectral bands are chosen by looking for "hot spots" in the correlation heat map. The method was applied both on observed spectra collected with the ASD spectrometer and the spectra simulated with the SNICAR model [*Flanner et al.*, 2007].

3.5. Radiative Forcing Calculation

Instantaneous RF (iRF) refers to an instantaneous change in net (down minus up) radiative flux (shortwave plus long wave, in W/m^2) due to an imposed change [*Myhre et al.*, 2013]. We refer herewith to iRF at top of surface (TOS) as the net change in upwelling irradiance due to the deposition of light-absorbing impurities in snow.

The iRF is here computed using a simple method based on field measurements of spectral irradiance $E(\lambda)$ ($W\,m^{-2}\,nm^{-1}$), calculated from observed radiance $L(\lambda)$ ($W\,m^{-2}\,sr^{-1}\,nm^{-1}$), using the formula $E(\lambda) = \pi L(\lambda)$, therefore assuming a Lambertian spectral response of snow. The method consists of calculating the spectral difference between the irradiance of "pure" snow $E_{ps}(\lambda)$ and the irradiance of a snow containing light-absorbing impurities $E_{MD}(\lambda)$, and then calculating the integrated instantaneous RF (iiRF) across the range from 350 to 850 nm. In formula, it can be expressed as

$$\mathrm{iiRF} = \sum_{350\mathrm{nm}}^{850\mathrm{nm}} \mathrm{iRF}(\lambda)\Delta\lambda = \sum_{350\mathrm{nm}}^{850\mathrm{nm}} E_{ps}(\lambda) - E_{MD}(\lambda)\Delta\lambda$$

The method is similar to that proposed by *Painter et al.* [2012b], but it differs from that since it does not depend on simulations of the spectral reflectance of snow. Although very simple, our method relies on the availability of snow cover with different concentration of MD and pure snow patches. This represents a limitation in the applicability in vast areas but allows direct observation of iRF values to compare with satellite observations and radiative transfer model simulations.

4. Results and Discussion

4.1. Mineral Dust Determination

MD concentrations determined by Coulter Counter (CC) and through the gravimetric method (GM) are reported for each sample in Table 1. The marked difference between the two methods can be ascribed to the different size intervals of the two measurements: CC techniques measured only particles between 1 and 30 μm, while the GM measured bulk particle weight.

Size distribution of fine particles determined by CC (an example in Figure 3) showed lognormal features with a main mode peaking at ~7 μm on average. This can be considered the mode of MD transported from North

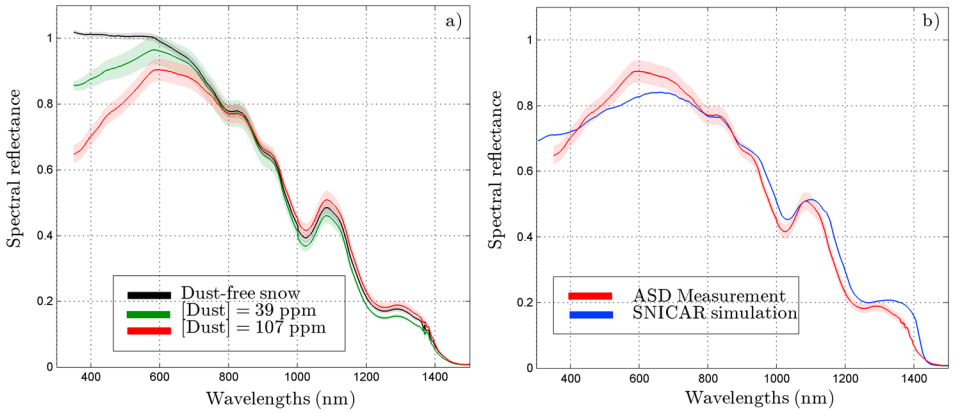

Figure 4. (left) Measured spectral reflectance (ASD Field Spec) for a control (C1) and two dust samples (DS6 and DS7). (right) Comparison between observed (red line) and simulated (blue line) reflectance (SNICAR model) for the sample DS6. In both plots, shaded areas represent the standard deviation.

Africa. Another mode is present in both samples and controls, starting at 18–20 μm. This coarse distributions are often associated with local transport of large particles produced by anthropic activity and/or local soil erosion, but a remote origin cannot be excluded [*Jeong et al.*, 2014].

4.2. Field Spectral Data and RT Model

Examples of reflectance spectra collected with the ASD field spectrometer at each sampling area are shown in Figure 4a. The presence of MD strongly decreases the albedo in the visible wavelengths, in particular, from 350 to ~800 nm. Beyond 800 nm, the effect of MD is negligible, since in this wavelength range, the impact of snow grain size is major [*Warren*, 1982]. This is in agreement with the simulation analysis conducted with the SNICAR model. Figure 5 shows examples of the hemispherical albedo simulated at different concentrations of MD (left) and different snow grain size (right). The plots point out the different effect of MD (size class from 5 to 10 μm) and grain size, in particular, the effect of MD is concentrated approximately between 350 and 1000 nm, while the effect of increasing grain size is observed for larger wavelengths, above 1000 nm.

The presence of MD in snow decreases its albedo in the visible wavelengths up to 40% for sample 6 which contains the major MD mass (CC: 107.4 ppm and GM: 325 ppm). Despite still few papers show observed reflectance spectra just after natural depositions of impurities, our data showed to be consistent with observation of MD on snow in literature [e.g., *Painter et al.*, 2007]. Conversely, marked differences were found with respect to spectra of BC on snow [i.e., *Hadley and Kirchstetter*, 2012], since in that case the decrease in albedo is more homogeneous among visible spectrum. Comparisons with the SNICAR simulations (Figure 4b) show that the model slightly underestimates the effect of MD for visible wavelengths, in particular, between 350 and 420 nm, and it overestimates the effect from 420 to 800 nm. The deviation between observed and simulated reflectance may be due to the upper boundary of SNICAR

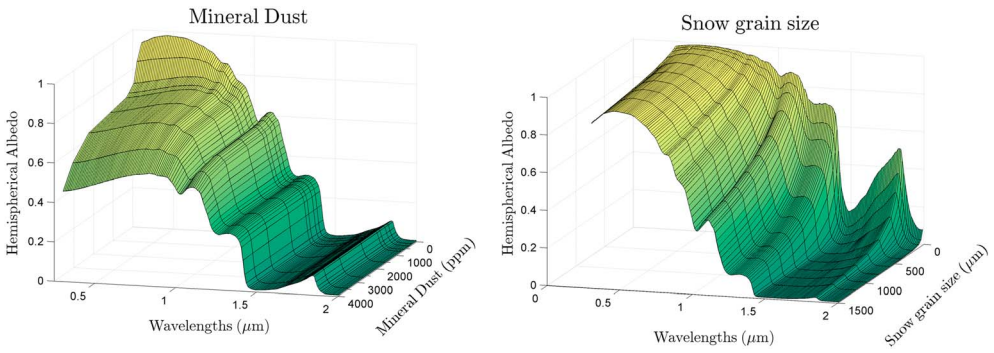

Figure 5. Snow hemispherical albedo simulated with the SNICAR model [*Flanner et al.*, 2007]. (left) SNICAR model was run varying MD concentration from 0 to 4000 ppm (size class: 5.0–10.0 μm). (right) SNICAR model was run varying snow grain size.

in particle dimension. In fact, even particles larger than 10 μm can in principle affect snow albedo by magnifying the absorption in visible wavelengths. This is not taken into account in the model formulation. In this respect, the difference between the MD concentration determined between the GM and CC indicated the presence of MD particles beyond the size range of the CC, as reported also in literature [*Katra et al.*, 2014]. This allows us to propose a first explanation regarding the SNICAR deviations with respect to the measured spectra.

Another possible source of mismatch between observed and simulated spectra is the different physical variable represented. In fact, the collection of measurements with a bare optical fiber implies observing an hemispherical conical reflectance [*Schaepman-Strub et al.*, 2006], while the SNICAR model simulates a bihemispherical reflectance. This can, in principle, affect a complete overlapping of the two reflectance.

In some cases, reflectance exceeded the value of 1, and it was impossible to compare observed and simulated data. This feature has often been found in literature [*Painter and Dozier*, 2004; *Schaepman-Strub et al.*, 2006; *Carmagnola et al.*, 2013] and was ascribed to the bidirectional effect that often occurs in surfaces such as snow [*Giardino and Brivio*, 2003; *Painter and Dozier*, 2004; *Schaepman-Strub et al.*, 2006]. However, as reported in literature, we do not expect this feature to affect the possibility of calculating spectral indices from the reflectance, in particular, for indices that operate in visible wavelengths where the bidirectional effect is more homogeneous [*Painter and Dozier*, 2004].

4.3. Definition of the Snow Darkening Index (SDI)

A nonlinear model (rational polynomial fitting) was chosen to account for the saturation effect in the decreasing of the albedo observed during the preliminary sensitivity analysis of the SNICAR simulations. Various linear and nonlinear models were applied to fit the simulated and observed data, but rational fitting produced the best results in terms of R^2. Furthermore, regarding SNICAR simulations, a rational model better approximated the dependence of SDI on MD concentration (Figure 8c). The model structure can be expressed in formula:

$$f(x) = \frac{p_1 x + p_2}{x + q_1}$$

where p_1, p_2, and q_1 are the parameters of the model, and x represents the concentration of MD obtained from the Coulter Counter determination.

From Figure 6 it is possible to identify which wavelengths combination generates the hot spot of highest correlation. Although different hot spots are displayed, we selected red (from 640 to 670 nm) and green (from 550 to 590 nm) wavelengths because they are spectral channels typically integrated in satellite sensors, they allow good applicability of the spectral index, and they are not influenced by snow grain size but enhance a spectral feature of MD in snow. This correlation hot spot was found in both the measured and simulated data sets. The SDI was then formalized as follows:

$$\mathrm{SDI} = \frac{\rho(640;670\ \mathrm{nm}) - \rho(550;590\ \mathrm{nm})}{\rho(640;670\ \mathrm{nm}) + \rho(550;590\ \mathrm{nm})}$$

In Figure 7a we show the best model obtained from the set of nonlinear ordinary least squares (nOLS) regressions between MD concentration using the CC method and combination of reflectance collected with the ASD spectrometer in the 10 sampling areas at the Artavaggio plains. In Figure 7b we show the linear regression between the Snow Darkening Index (SDI) calculated from the ASD data and from the SNICAR simulated data. The correlation between the data ($R^2 = 0.86$) means that despite some differences found between observed and simulated spectra (section 4.2), the SDI is able to capture the overall variability in MD concentration from different source of data. To validate the hypothesis that large particles (i.e., diameter > 30 μm) also affect snow albedo, we calculated the differences between the gravimetric method (GM) and the Coulter Counter (CC) measurements, which reflect the amount of large particles among snow samples. Then we calculated the correlation between this difference and the difference of SDI calculated from the ASD band and from the SNICAR model. The nonlinear correlation found in data (rational fit, $R^2 = 0.95$) states that as the concentration of large particles increases, the deviation between observed and simulated SDI first increases and then shows a saturation effect.

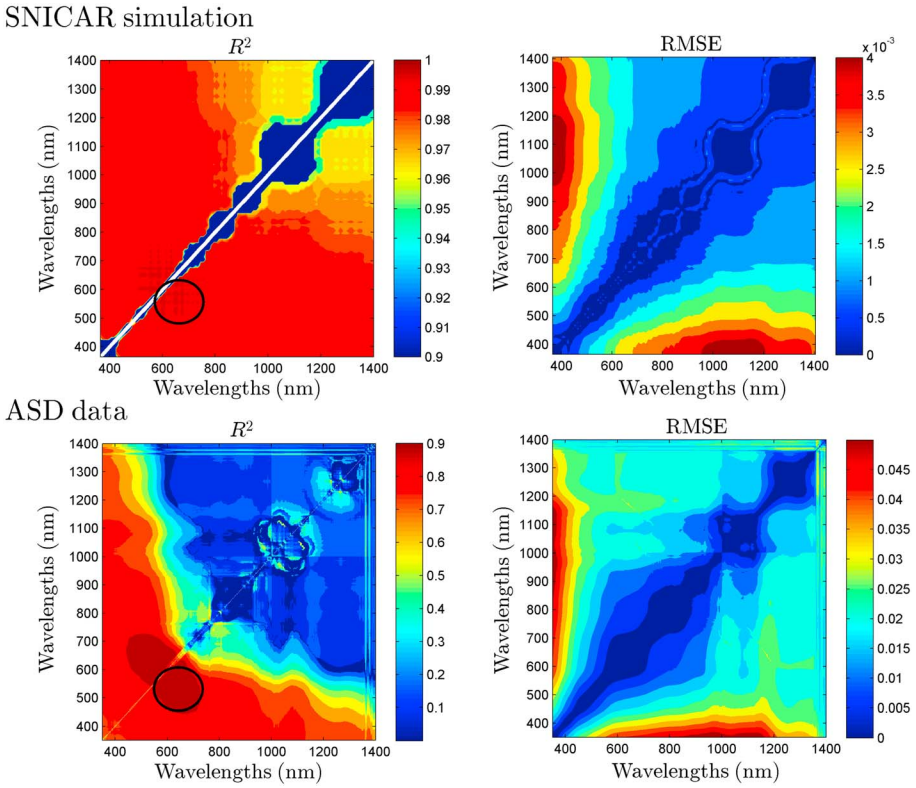

Figure 6. (top) Correlation heat map of R^2 and root-mean-square error (RMSE) resulting from nonlinear ordinary least squares (nOLS) between SNICAR-simulated reflectance and MD concentration of samples (determined with CC). (bottom) Correlation heat map of R^2 and RMSE resulting from nOLS between ASD reflectance and MD concentration (determined with CC).

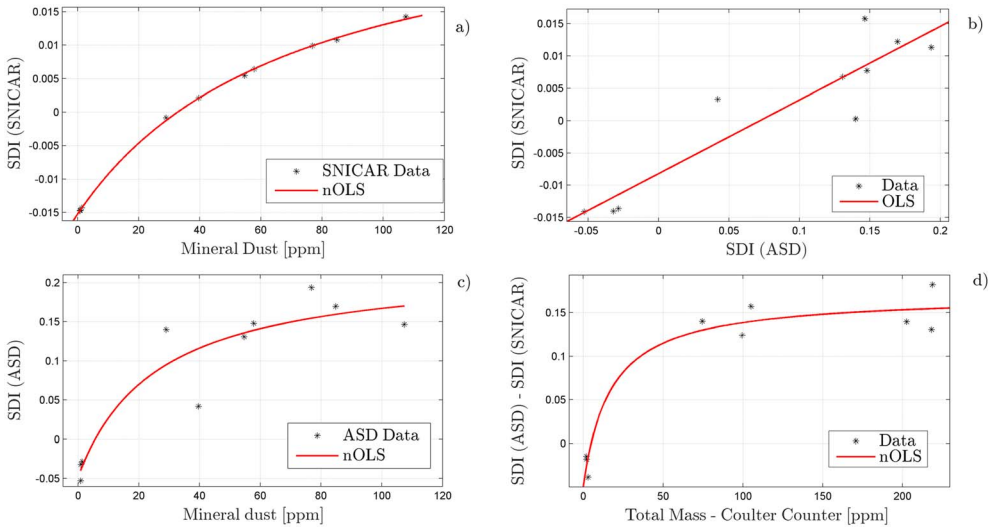

Figure 7. Nonlinear OLS regression between MD concentration and SDI values calculated from (a) SNICAR simulations. Linear OLS regression between the SDI calculated from observed ASD data and (b) simulated SNICAR data. Nonlinear OLS regression (rational fit) between MD concentrations obtained with the Coulter Counter (CC) versus the Snow Darkening Index (SDI) calculated on the hyperspectral data collected with the (c) ASD spectrometer. Nonlinear OLS regression between the differences of MD concentration obtained from GM and CC method versus the differences of the SDI calculated from SNICAR and observed with the ASD radiometer (Figure 7c).

Table 2. Review of the Model Structure, Coefficients (With 95% Confidence Bounds), and Goodness of Fit in Terms of Coefficient of Determination (R^2), Adjusted Coefficient of Determination (R^2_{adj}), Root-Mean-Square Error (RMSE), and Sum Square Error (SSE) of the Plots Shown in Figures 7 and 11

Variables	Type of Fit	Model Structure	Coefficients (with 95% Confidence Bounds)	R^2	R^2_{adj}	RMSE	SSE
MD versus SDI (ASD)	Rational	$f(x) = \frac{p_1 x + p_2}{x + q_1}$	$p_1 = 0.22$ (0.04, 0.41) $p_2 = -1.24$ (−3.87, 1.38) $q_1 = 26$ (−35.98, 87.97)	0.87	0.84	0.037	0.009
SDI (ASD) versus SDI (SNICAR)	Linear	$f(x) = p_1 x + p_2$	$p_1 = 0.11$ (0.08, 0.15) $p_2 = -0.01$ (−0.013, −0.003)	0.86	0.84	0.005	0.002
MD (CC) versus SDI (SNICAR)	Rational	$f(x) = \frac{p_1 x + p_2}{x + q_1}$	$p_1 = 0.03$ (0.03, 0.036) $p_2 = -1.08$ (−1.21, −0.96) $q_1 = 71.1$ (62.3, 79.9)	0.99	0.99	0.00025	4.557e-07
SDI (ASD) versus SDI (UAV)	Linear	$f(x) = p_1 x + p_2$	$p_1 = 0.14$ (0.09, 0.18) $p_2 = -0.05$ (−0.05, −0.04)	0.83	0.81	0.006	0.001
GM-CC versus SDI (ASD)-SDI (SNICAR)	Rational	$f(x) = \frac{p_1 x + p_2}{x + q_1}$	$p_1 = 0.17$ (0.1, 0.24) $p_2 = -0.83$ (−2.19, 0.52) $q_1 = 16.9$ (−31.52, 65.28)	0.95	0.94	0.022	0.003

Clearly, SDI and integrated snow broadband albedo have a linear inverse correlation (data not shown), and it is important to underline that SDI is built on a spectral feature of MD in snow. As a consequence, a decrease in albedo due to increasing grain size in snow without MD will not affect SDI values but will, nevertheless, decrease snow albedo.

Table 2 shows a review of the model structures, coefficients (with 95% confidence bounds), and goodness of fit in terms of coefficient of determination (R^2), adjusted coefficient of determination (R^2_{adj}), root-mean-square error (RMSE), and sum square error (SSE).

Figure 8 shows the combined effect on SDI of increasing MD concentration and snow grain size using the simulations from the SNICAR model. A global spline interpolator was applied for representation purposes. The interaction of increasing MD concentration and increasing of individual snow grain size causes an amplified effect on snow albedo and hence on SDI values. It is well known that light-absorbing impurities cause an increase in snow grain size due to enhanced absorption [*Warren and Wiscombe*, 1980; *Meinander et al.*, 2014]; because of this feature, the two effects are very difficult to separate, and SDI showed a nonlinear response to grain size increase in snow containing MD (Figure 8).

4.4. RF Estimation

An example of the radiative forcing (RF) computed at the Artavaggio site for two sampling areas containing 39 ppm and 107 ppm of MD measured with the CC method is shown in Figure 9. Figure 9 (left) shows the upwelling spectral irradiances (W/m^2) (one control, C1, and two dust samples, DS6 and DS7) measured with the ASD spectrometer. The spectral difference (i.e., the instantaneous RF) between these two irradiances represents a direct proxy of the amount of solar radiation absorbed in the snowpack due to the present of MD deposition. The integration of the iRF between 350 and 850 nm gives the integrated instantaneous RF (iiRF) in W/m^2, which was estimated as equal to 103.2 W/m^2 for the DS with 39 ppm and 153.9 W/m^2 for the DS with 107 ppm. We also show the spectral dependence of iRF. In particular, we observed that the iRF increases from 350 to 450 nm and then decreases in

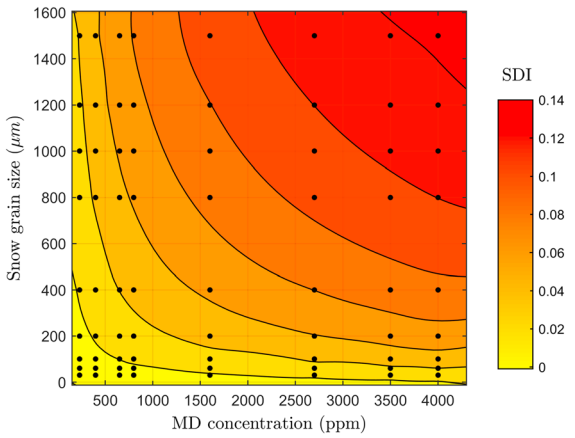

Figure 8. Representation of the SDI index as a function of mineral dust (MD) concentration (ppm) and snow grain size (μm). The black dots are obtained from SNICAR simulation, and colored facets are a global spline interpolator applied for representation purposes.

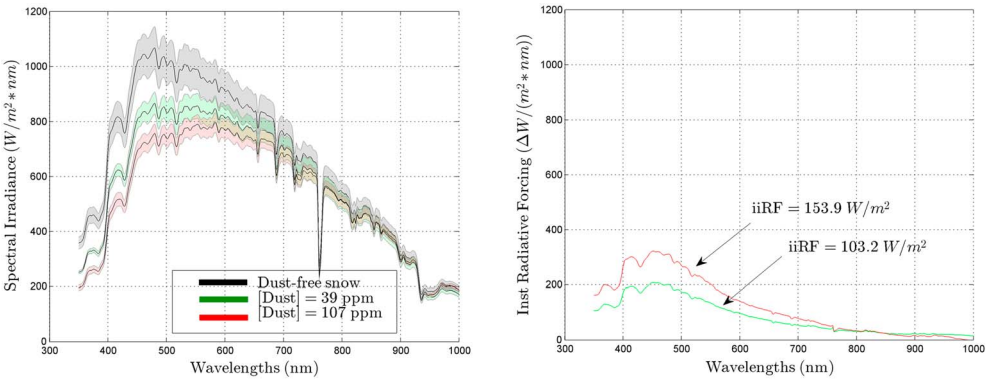

Figure 9. (left) Spectral irradiances of the sample containing 0.92 ppm of MD (black line), snow containing 39 ppm (green line), and 107 ppm (red line) of MD. (right) Instantaneous radiative forcing iRF(λ) of snow containing different concentrations of MD. The samples are the same as shown in Figure 4.

longer wavelengths, reaching approximately zero at 1000 nm. This spectral dependence is very specific for the MD impact on snow radiative properties. Possible difficulties in the application of this method lie in the choice of the sampling areas in which to measure the spectral irradiance and the availability of adjacent snow patches with comparable slope and aspect showing different concentrations of impurities. Previous works [*Painter et al.*, 2012b, 2013b; *Kaspari et al.*, 2014, 2015] found similar values for iiRF of light-absorbing impurities in snow. We remark that MD has a strong positive forcing effect when deposited on snow. The instantaneous RF from MD can be higher than that generated by BC depositions on snow, as recently suggested by *Kaspari et al.* [2014] from a modeling approach in the Himalayan region. Still a lot of uncertainties exist regarding the RF of BC and MD in snow. A critical point regards methodologies followed by different authors; they should be unified in order to effectively compare results from different observational and simulation studies.

The amount of solar radiation absorbed in the snowpack because of the presence of MD can be directly thermalized through the media enhancing its temperature. If no new snowfall occurs, this process can significantly accelerate the melting of snow [*Painter et al.*, 2010], anticipating snow retreat in mountain areas, altering local radiative balance, and shifting vegetation phenology. Furthermore, the well-known snow albedo feedback [*Hansen and Nazarenko*, 2004] can here operate in the following way: as the snowmelt is increased by the presence of MD, the MD itself is concentrated by the melting in nearly flat areas in mountain regions. In this study, we present only an instantaneous view of the process. During the 2013–2014 winter, the European Alpine area experienced intense snowfalls; in this way, the radiative effect of MD may be damped by the presence of fresh snow above the MD layers. But during the melting season, the MD layers reemerge and enhance the absorption of solar radiation. This process may also affect underlying ice in the accumulation zone of Alpine mountain glaciers.

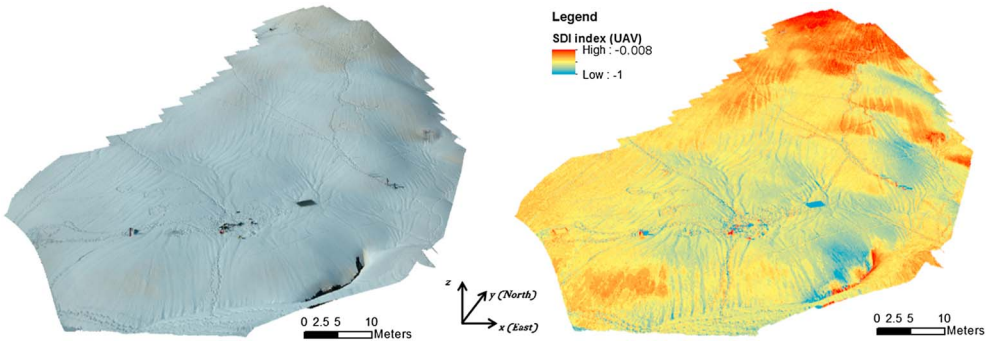

Figure 10. (left) Orthomosaic of UAV-RGB data for the first flight draped on the digital surface model (DSM) of the area. (right) Maps of SDI index calculated as the normalized ratio between the red and green channel of the Canon s100.

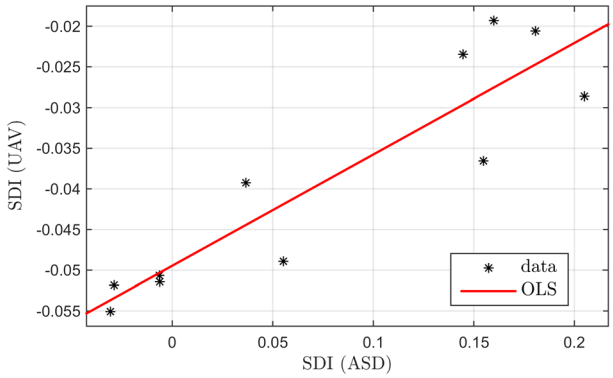

Figure 11. Linear OLS regression between the SDI calculated from ASD data and from UAV data ($R^2 = 0.83$) at each sampling area of the Artavaggio plains.

4.5. Snow Darkening Index (SDI) Applications

The RGB digital numbers (DNs) of the camera on board the UAV were algebraically combined to reproduce the SDI index as follows: (DN(red)-DN(green))/(DN (red) + DN(green)). The values of SDI estimated from UAV were then compared to those observed from the ground using the ASD spectrometer.

Atmospherically and topographically corrected Landsat OLI top of surface (TOS) reflectances in band 3 (0.525–0.600 μm) and band 4 (0.630–0.680 μm) were also algebraically combined to calculate the SDI index as follows: $(\rho(B4_{TOS}) - \rho(B3_{TOS}))/(\rho(B4_{TOS}) + \rho(B3_{TOS}))$.

SDI values were calculated only in those areas covered by snow and ice. The classes were produced using a supervised classification approach (maximum likelihood) of the nine OLI bands. The classification was applied only in mountain areas of the Landsat tile using the three training classes: snow, vegetation, and urban.

Once the SDI map was created, it was classified in terms of exposure of the slopes (eight classes: NNE, EEN, EES, SSE, SSW, WWS, WWN, and NNW) using the ASTER GDEM, to analyze whether south facing slopes were more impacted by the MD transport because of enhanced melting due to higher solar irradiance.

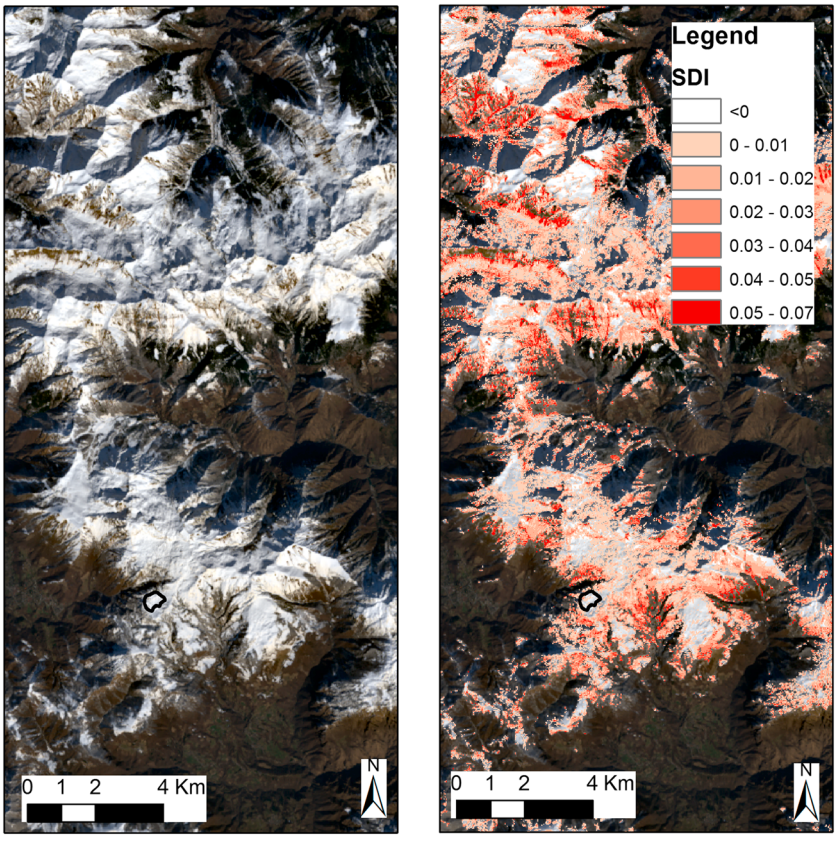

Figure 12. (a) Landsat 8 image and (b) SDI map of the Artavaggio plains. The black polygon in the maps represents the area covered by the UAV survey.

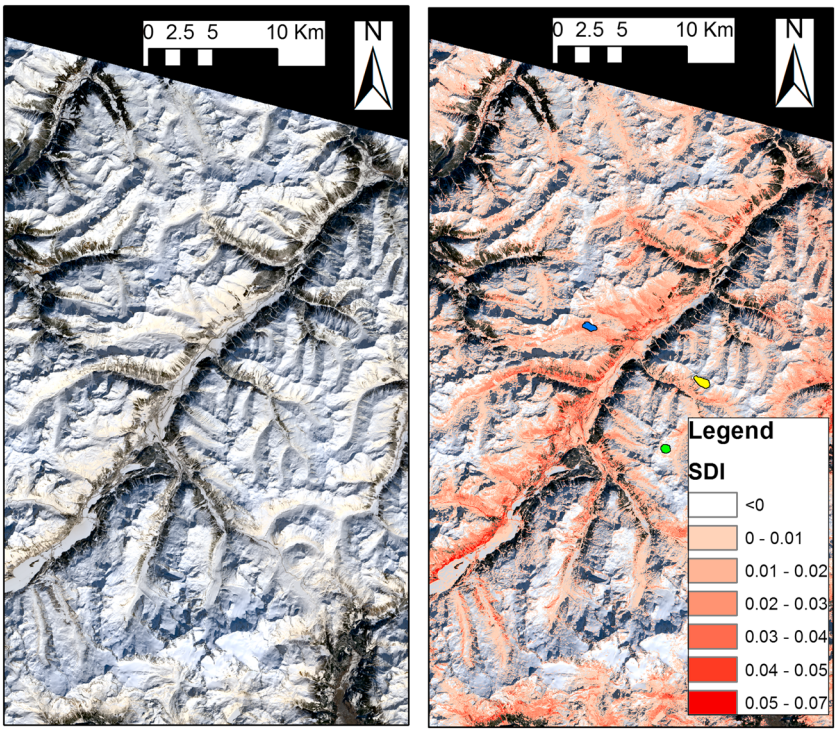

Figure 13. (a) Landsat 8 OLI image and (b) SDI maps of the central European Alps. Three regions of interest (ROI) showing different values of SDI were selected in the Engadine region (Switzerland). ROI color legend: Blue = ROI-2, yellow = ROI-1, and green = ROI-0.

Figure 10 shows the SDI map derived from UAV data on the Artavaggio plains. Spatial variability of dust patches is clearly visible in the RGB orthomosaic (Figure 10), and it is enhanced in the SDI map. The map shows both fresh and reemerging layers of MD in snow and represents a simple way to detect MD depositions in snow by exploiting the different reflectance in visible channels. The map shows a south facing slope where the concentrations of impurities in snow are naturally higher in the Northern Hemisphere because of the longer exposition to direct solar radiation. This indicates that slope morphology plays an important role in enhancing or dampening the effect of MD on snow albedo. In fact, small basins in high-altitude areas can increase the concentration of MD in snow during the melting season, thus accelerating the nonlinear response of snow. Possible influence of other light-absorbing impurities (e.g., BC) are not tested here since we focused on MD, but they may be contributing to the overall reduction of reflectance.

Figure 11 shows the linear regression ($R^2 = 0.83$) between the SDI calculated in each sampling area of the UAV orthomosaic and the SDI calculated from ASD spectra. We found a linear correlation that assesses the possibility of calculating the SDI also from RBG images to spatially represent MD deposition in snow. SDI values calculated from UAV and ASD data differ more than an order of magnitude, this feature is due to the fact that SDI from UAV was calculated combining raw DN values of the RGB images.

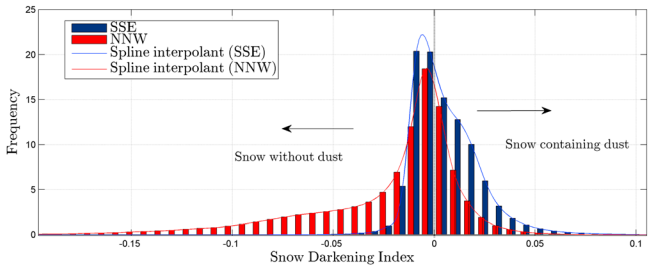

Figure 14. Frequency distribution of SDI for the central European Alps classified in class of slope exposition: South southeast (SSE) and north northeast (NNW). The histograms show that south facing slopes have higher SDI values than the north facing slopes.

Results from the SDI calculation on Landsat OLI bands are shown in Figures 12 and 13. Figure 12 shows the Landsat image and the

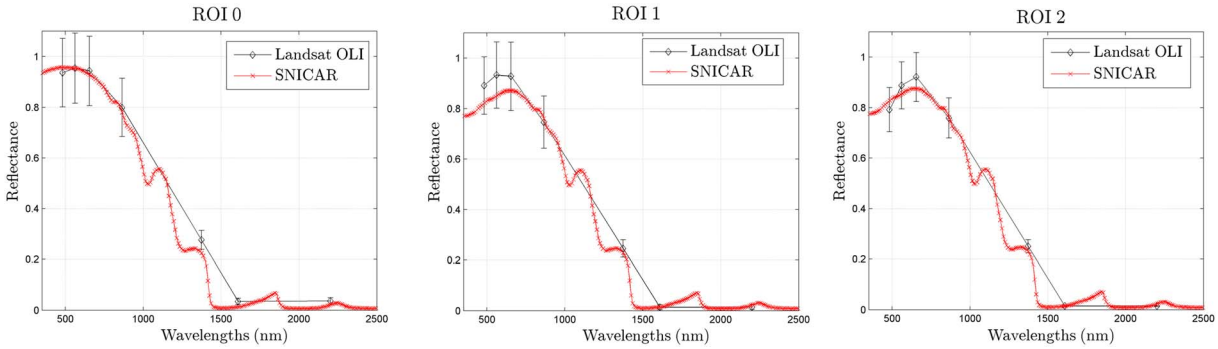

Figure 15. Comparison between Landsat and SNICAR reflectance for the three regions of interest (ROI) shown in Figure 10.

SDI map of the Artavaggio plains. The black polygon in the maps represents the area covered by the UAV survey. The coarse resolution of the Landsat image (30 m) does not allow the entire capture of all the spatial variability of MD due to snow micromorphology as compared with the UAV resolution (Figure 10), although some spatial variability of SDI is still visible in Landsat data. In Figure 13, a larger area within the central European Alps is examined. The presence of MD in snow is visible from the Landsat true color representation, and it is well represented in the SDI map, which reveals portions of lower and higher MD deposition differently located in the catchment.

Figure 14 shows the frequency distribution of the SDI index in south southeast (SSE) and in the north northwest (NNW) classes of slope exposure for the mountain area within the Landsat tile. SDI assumes higher values in SSE slopes with respect to NNW slopes. Since the image was topographically corrected using the ATCOR code, the effect of shadows does not influence SDI values. The separation of the two distributions shows that in this case, south facing slopes also have, on average, higher SDI values, suggesting that both the provenance of the MD plume and longer exposition to solar radiation manifest their effects at different scales. Similar pattern was observed in broadband albedo and RF values in Colorado [*Painter et al.*, 2013b], where lower RF values were found in the high north facing cirques, where less direct radiation slows the metamorphism of snow; higher RF values were found on southeast facing slopes at the lowest elevations.

In the upper left region of the central European Alps (Engadina, Switzerland), we selected three regions of interest (ROI), showing different SDI values comparable with those observed in the study area: from low (ROI-0) to medium (ROI-1) and high (ROI-2) SDI values. For each ROI, we extracted the mean and standard deviation of reflectance from the Landsat image. In Figure 15 we show the spectra of atmospherically topographically corrected reflectance for the three ROI, overlapped with SNICAR simulations that showed similar SDI values. Although Landsat has a lower spectral resolution with respect to that of the SNICAR model, the plot from ROI 0 shows a good agreement between observed and simulated reflectance. The plot from ROI-1 shows an offset between the reflectance, and the plot from ROI-2, shows a behavior similar to that observed between ASD and SNICAR reflectance (Figure 4b). In fact, the SNICAR model in this case also slightly underestimates the effect of MD on snow reflectance for wavelengths lower than 600 nm.

Also to be noted is that for the Landsat spectra, we found reflectance values that exceeded the value of 1, thus confirming the feature reported in previous literature [*Painter and Dozier*, 2004; *Schaepman-Strub et al.*, 2006; *Carmagnola et al.*, 2013; *Pope and Rees*, 2014] and ascribed to the strong forward scattering of snow.

5. Conclusions

In this paper, we propose a simple methodology for mapping light-absorbing impurities such as mineral dust (MD) in snow using optical data that range from hyperspectral sensor to multispectral and RGB images. We developed the method through a field campaign aimed at quantifying the actual impact of MD on snow albedo after a significant MD transport that reached the European Alps from the Saharan desert during

the spring of 2014. We compared high-resolution reflectance spectra (collected with an ASD field spectrometer) with reflectance simulated by parameterizing a physically based radiative transfer model (SNICAR). Differences between observed and simulated data were ascribed to the effect of particles with diameters above 30 μm that are not included in the SNICAR model but nevertheless can increase light absorption. Using the hot spots method, it was possible to find a model based on maximization of the coefficient of regression (R^2) and minimization of the root-mean-squared error (RMSE). Through these rules it was found that the normalized ratio between red and green wavelengths (the Snow Darkening Index, SDI) is highly correlated with the MD concentration. We claim that this may help to gain reasonable estimates of light-absorbing impurities, such as MD, in snow.

Multiscale observations with an Unmanned Aerial Vehicle (UAV) and Landsat OLI satellite sensor showed a significant impact of MD on snow albedo. This allowed us to spatially represent the SDI at local and regional scales in the European Alps. The wide applicability of the SDI will allow mapping of past events of MD deposition on snow from different sensors that range from airborne and terrestrial digital cameras [i.e., *Dumont et al.*, 2011] to different satellite sensors (Landsat, MODIS, etc.), generating, for example, SDI time series to study postdepositional dynamics of MD on snow and ice.

Furthermore, we propose a simple method to estimate instantaneous radiative forcing (iRF) of MD in snow, based on the difference between spectral irradiances of pure snow and snow containing a significant amount of MD. Our iRF estimations are comparable with those found in previous literature and represent an opportunity to directly estimate iRF from field spectral measurements, which is very useful for validating global climate models and radiative transfer models.

The impact of light-absorbing impurities on snow radiative properties represents an active field of research in atmosphere and cryosphere sciences, with many uncertainties in model simulations. Our results show the first evidence that MD strongly impacts snow reflectance in the European Alps, where Saharan MD events are very frequent in the spring season. Furthermore, climate change is known to alter meteo-climatic patterns (e.g., North Atlantic Oscillation, NAO), eventually leading to stronger and more frequent MD transport toward the European Alpine chain, and this may result in an early snowmelt and variations in local radiative balances.

Acknowledgments

The research was supported by the SINOPIAE project funded by the Regione Lombardia. Data used in this paper will be made available upon request to first author e-mail address (b.dimauro@campus.unimib.it). The authors wish to thank C. Giardino (CNR-IREA) for lending the ASD-Field Spec and for help with Landsat 8 topo-atmospheric correction with ATCOR. Furthermore, we thank the Aermatica team, S. Cogliati, M. Fagnani, E. Bolzacchini, and M. Casati for their help in organizing the field campaign. We thank the reviewers and the Editor for their work and their useful comments and suggestions that helped us in improving the quality of the manuscript.

References

Albani, S., N. M. Mahowald, A. T. Perry, R. A. Scanza, C. S. Zender, N. G. Heavens, V. Maggi, J. F. Kok, and B. L. Otto-Bliesner (2014), Improved dust representation in the Community Atmosphere Model, *J. Adv. Model. Earth Syst.*, doi:10.1002/2013MS000279.

Aoki, T., K. Kuchiki, M. Niwano, Y. Kodama, M. Hosaka, and T. Tanaka (2011), Physically based snow albedo model for calculating broadband albedos and the solar heating profile in snowpack for general circulation models, *J. Geophys. Res.*, *116*, D11114, doi:10.1029/2010JD015507.

Basart, S., C. Pérez, S. Nickovic, E. Cuevas, and J. M. Baldasano (2012), Development and evaluation of the BSC-DREAM8b dust regional model over Northern Africa, the Mediterranean and the Middle East, *Tellus B*, *64*, doi:10.3402/tellusb.v64i0.18539.

Bauer, E., and A. Ganopolski (2014), Sensitivity simulations with direct shortwave radiative forcing by aeolian dust during glacial cycles, *Clim. Past*, *10*(4), 1333–1348, doi:10.5194/cp-10-1333-2014.

Berk, A., L. S. Bernstein, and D. C. Robertson (1989), MODTRAN: A moderate resolution model for LOWTRAN 7.

Bond, T. C., et al. (2013), Bounding the role of black carbon in the climate system: A scientific assessment, *J. Geophys. Res. Atmos.*, *118*, 5380–5552, doi:10.1002/jgrd.50171.

Brandt, R. E., S. G. Warren, and A. D. Clarke (2011), A controlled snowmaking experiment testing the relation between black carbon content and reduction of snow albedo, *J. Geophys. Res.*, *116*, D08109, doi:10.1029/2010JD015330.

Bryant, A. C., T. H. Painter, J. S. Deems, and S. M. Bender (2013), Impact of dust radiative forcing in snow on accuracy of operational runoff prediction in the upper Colorado river basin, *Geophys. Res. Lett.*, *40*, 3945–3949, doi:10.1002/grl.50773.

Carmagnola, C. M., et al. (2013), Snow spectral albedo at Summit, Greenland: Measurements and numerical simulations based on physical and chemical properties of the snowpack, *Cryosphere*, *7*(4), 1139–1160, doi:10.5194/tc-7-1139-2013.

Claquin, T., et al. (2003), Radiative forcing of climate by ice-age atmospheric dust, *Clim. Dyn.*, *20*(2-3), 193–202, doi:10.1007/s00382-002-0269-1.

Clarke, A. D., and K. J. Noone (1985), Soot in the Arctic snowpack: A cause for perturbations in radiative transfer, *Atmos. Environ.*, *19*(12), 2045–2053, doi:10.1016/0004-6981(85)90113-1.

Conway, H., A. Gades, and C. F. Raymond (1996), Albedo of dirty snow during conditions of melt, *Water Resour. Res.*, *32*(6), 1713–1718, doi:10.1029/96WR00712.

Dagsson-Waldhauserova, P., O. Arnalds, H. Olafsson, J. Hladil, R. Skala, T. Navratil, L. Chadimova, and O. Meinander (2015), Snow–Dust Storm: Unique case study from Iceland, March 6–7, 2013, *Aeolian Res.*, *16*, 69–74, doi:10.1016/j.aeolia.2014.11.001.

De Angelis, M., and A. Gaudichet (1991), Saharan dust deposition over Mont Blanc (French Alps) during the last 30 years, *Tellus B*, *43*(1), doi:10.3402/tellusb.v43i1.15246.

Delmonte, B., J. Petit, and V. Maggi (2002), Glacial to Holocene implications of the new 27000-year dust record from the EPICA Dome C (East Antarctica) ice core, *Clim. Dyn.*, *18*(8), 647–660, doi:10.1007/s00382-001-0193-9.

Doherty, S. J., C. Dang, D. A. Hegg, R. Zhang, and S. G. Warren (2014), Black carbon and other light-absorbing particles in snow of central North America, *J. Geophys. Res. Atmos.*, *119*, 12,807–12,831, doi:10.1002/2014JD022350.

Dumont, M., P. Sirguey, Y. Arnaud, and D. Six (2011), Monitoring spatial and temporal variations of surface albedo on Saint Sorlin Glacier (French Alps) using terrestrial photography, *Cryosphere*, *5*, 759–771, doi:10.5194/tc-5-759-2011.

Dumont, M., E. Brun, G. Picard, M. Michou, Q. Libois, J.-R. Petit, M. Geyer, S. Morin, and B. Josse (2014), Contribution of light-absorbing impurities in snow to Greenland's darkening since 2009, *Nat. Geosci.*, *7*(7), 509–512, doi:10.1038/ngeo2180.

Fava, F., R. Colombo, S. Bocchi, M. Meroni, M. Sitzia, N. Fois, and C. Zucca (2009), Identification of hyperspectral vegetation indices for Mediterranean pasture characterization, *Int. J. Appl. Earth Obs. Geoinf.*, *11*(4), 233–243, doi:10.1016/j.jag.2009.02.003.

Field, J. P., J. Belnap, D. D. Breshears, J. C. Neff, G. S. Okin, J. J. Whicker, T. H. Painter, S. Ravi, M. C. Reheis, and R. L. Reynolds (2010), The ecology of dust, *Front. Ecol. Environ.*, *8*(8), 423–430, doi:10.1890/090050.

Flanner, M. G., and C. S. Zender (2005), Snowpack radiative heating: Influence on Tibetan Plateau climate, *Geophys. Res. Lett.*, *32*, L06501, doi:10.1029/2004GL022076.

Flanner, M. G., C. S. Zender, J. T. Randerson, and P. J. Rasch (2007), Present-day climate forcing and response from black carbon in snow, *J. Geophys. Res.*, *112*, D11202, doi:10.1029/2006JD008003.

Flanner, M. G., C. S. Zender, P. G. Hess, N. M. Mahowald, T. H. Painter, V. Ramanathan, and P. J. Rasch (2009), Springtime warming and reduced snow cover from carbonaceous particles, *Atmos. Chem. Phys.*, *9*(7), 2481–2497, doi:10.5194/acp-9-2481-2009.

Franzén, L. G., M. Hjelmroos, P. Kållberg, A. Rapp, J. O. Mattsson, and E. Brorström-Lundén (1995), The Saharan dust episode of south and central Europe, and northern Scandinavia, March 1991, *Weather*, *50*(9), 313–318, doi:10.1002/j.1477-8696.1995.tb06139.x.

Gautam, R., N. C. Hsu, W. K.-M. Lau, and T. J. Yasunari (2013), Satellite observations of desert dust-induced Himalayan snow darkening, *Geophys. Res. Lett.*, *40*, 988–993, doi:10.1002/grl.50226.

Giardino, C., and P. A. Brivio (2003), The application of a dedicated device to acquire bidirectional reflectance factors over natural surfaces, *Int. J. Remote Sens.*, *24*(14), 2989–2995, doi:10.1080/0143116031000094782.

Goudie, A. S., and N. J. Middleton (2001), Saharan dust storms: Nature and consequences, *Earth Sci. Rev.*, *56*(1–4), 179–204, doi:10.1016/S0012-8252(01)00067-8.

Hadley, O. L., and T. W. Kirchstetter (2012), Black-carbon reduction of snow albedo, *Nat. Clim. Change.*, *2*(6), 437–440, doi:10.1038/nclimate1433.

Hadley, O. L., C. E. Corrigan, T. W. Kirchstetter, S. S. Cliff, and V. Ramanathan (2010), Measured black carbon deposition on the Sierra Nevada snowpack and implication for snowpack retreat, *Atmos. Chem. Phys.*, *10*(15), 7505–7513, doi:10.5194/acp-10-7505-2010.

Hall, D. K., G. A. Riggs, and V. V. Salomonson (1995), Development of methods for mapping global snow cover using moderate resolution imaging spectroradiometer data, *Remote Sens. Environ.*, *54*(2), 127–140, doi:10.1016/0034-4257(95)00137-P.

Hansen, J., and L. Nazarenko (2004), Soot climate forcing via snow and ice albedos, *Proc. Natl. Acad. Sci. U.S.A.*, *101*(2), 423–428, doi:10.1073/pnas.2237157100.

Hansen, P. M., and J. K. Schjoerring (2003), Reflectance measurement of canopy biomass and nitrogen status in wheat crops using normalized difference vegetation indices and partial least squares regression, *Remote Sens. Environ.*, *86*(4), 542–553, doi:10.1016/S0034-4257(03)00131-7.

Helmert, J., B. Heinold, I. Tegen, O. Hellmuth, and M. Wendisch (2007), On the direct and semidirect effects of Saharan dust over Europe: A modeling study, *J. Geophys. Res.*, *112*, D13208, doi:10.1029/2006JD007444.

Hodson, A., et al. (2007), A glacier respires: Quantifying the distribution and respiration CO_2 flux of cryoconite across an entire Arctic supraglacial ecosystem, *J. Geophys. Res.*, *112*, G04S36, doi:10.1029/2007JG000452.

Immerzeel, W. W., P. D. A. Kraaijenbrink, J. M. Shea, A. B. Shrestha, F. Pellicciotti, M. F. P. Bierkens, and S. M. de Jong (2014), High-resolution monitoring of Himalayan glacier dynamics using unmanned aerial vehicles, *Remote Sens. Environ.*, *150*, 93–103, doi:10.1016/j.rse.2014.04.025.

Irons, J. R., J. L. Dwyer, and J. A. Barsi (2012), The next Landsat satellite: The Landsat Data Continuity Mission, *Remote Sens. Environ.*, *122*, 11–21, doi:10.1016/j.rse.2011.08.026.

Jacobson, M. Z. (2004), Climate response of fossil fuel and biofuel soot, accounting for soot's feedback to snow and sea ice albedo and emissivity, *J. Geophys. Res.*, *109*, D21201, doi:10.1029/2004JD004945.

Jeong, G. Y., J. Y. Kim, J. Seo, G. M. Kim, H. C. Jin, and Y. Chun (2014), Long-range transport of giant particles in Asian dust identified by physical, mineralogical, and meteorological analysis, *Atmos. Chem. Phys.*, *14*(1), 505–521, doi:10.5194/acp-14-505-2014.

Kaspari, S., T. H. Painter, M. Gysel, S. M. Skiles, and M. Schwikowski (2014), Seasonal and elevational variations of black carbon and dust in snow and ice in the Solu-Khumbu, Nepal and estimated radiative forcings, *Atmos. Chem. Phys.*, *14*(15), 8089–8103, doi:10.5194/acp-14-8089-2014.

Kaspari, S., S. M. Skiles, I. Delaney, D. Dixon, and T. H. Painter (2015), Accelerated glacier melt on Snow Dome, Mt. Olympus, Washington, USA due to deposition of black carbon and mineral dust from wildfire, *J. Geophys. Res. Atmos.*, *120*, 2793–2807, doi:10.1002/2014JD022676.

Katra, I., L. Arotsker, H. Krasnov, A. Zaritsky, A. Kushmaro, and E. Ben-Dov (2014), Richness and diversity in dust stormborne biomes at the southeast mediterranean, *Sci. Rep.*, *4*, 5265, doi:10.1038/srep05265.

Kaufman, Y. J., and C. Sendra (1988), Algorithm for automatic atmospheric corrections to visible and near-IR satellite imagery, *Int. J. Remote Sens.*, *9*(8), 1357–1381, doi:10.1080/01431168808954942.

Kutuzov, S., M. Shahgedanova, V. Mikhalenko, P. Ginot, I. Lavrentiev, and S. Kemp (2013), High-resolution provenance of desert dust deposited on Mt. Elbrus, Caucasus in 2009–2012 using snow pit and firn core records, *Cryosphere*, *7*(5), 1481–1498, doi:10.5194/tc-7-1481-2013.

Lawrence, D. M., et al. (2011), Parameterization improvements and functional and structural advances in Version 4 of the Community Land Model, *J. Adv. Model. Earth Syst.*, *3*, M03001, doi:10.1029/2011MS000045.

Li, J., G. S. Okin, S. McKenzie Skiles, and T. H. Painter (2013), Relating variation of dust on snow to bare soil dynamics in the western United States, *Environ. Res. Lett.*, *8*(4), 044,054, doi:10.1088/1748-9326/8/4/044054.

Lin, G., J. E. Penner, M. G. Flanner, S. Sillman, L. Xu, and C. Zhou (2014), Radiative forcing of organic aerosol in the atmosphere and on snow: Effects of SOA and brown carbon, *J. Geophys. Res. Atmos.*, *119*, 7453–7476, doi:10.1002/2013JD021186.

Liou, K. N., Y. Takano, C. He, P. Yang, L. R. Leung, Y. Gu, and W. L. Lee (2014), Stochastic parameterization for light absorption by internally mixed BC/dust in snow grains for application to climate models, *J. Geophys. Res. Atmos.*, *119*, 7616–7632, doi:10.1002/2014JD021665.

Lucieer, A., D. Turner, D. H. King, and S. A. Robinson (2014), Using an Unmanned Aerial Vehicle (UAV) to capture micro-topography of Antarctic moss beds, *Int. J. Appl. Earth Obs. Geoinf.*, *27*, 53–62, doi:10.1016/j.jag.2013.05.011.

Maher, B. A., J. M. Prospero, D. Mackie, D. Gaiero, P. P. Hesse, and Y. Balkanski (2010), Global connections between aeolian dust, climate and ocean biogeochemistry at the present day and at the last glacial maximum, *Earth Sci. Rev.*, *99*(1-2), 61–97, doi:10.1016/j.earscirev.2009.12.001.

Mahowald, N. M., A. R. Baker, G. Bergametti, N. Brooks, R. A. Duce, T. D. Jickells, N. Kubilay, J. M. Prospero, and I. Tegen (2005), Atmospheric global dust cycle and iron inputs to the ocean, *Global Biogeochem. Cycles*, *19*, GB4025, doi:10.1029/2004GB002402.

Mahowald, N., S. Albani, J. F. Kok, S. Engelstaeder, R. Scanza, D. S. Ward, and M. G. Flanner (2013), The size distribution of desert dust aerosols and its impact on the Earth system, *Aeolian Res.*, doi:10.1016/j.aeolia.2013.09.002.

McConnell, J. R., R. Edwards, G. L. Kok, M. G. Flanner, C. S. Zender, E. S. Saltzman, J. R. Banta, D. R. Pasteris, M. M. Carter, and J. D. W. Kahl (2007), 20th-century industrial black carbon emissions altered Arctic climate forcing, *Science*, *317*(5843), 1381–1384, doi:10.1126/science.1144856.

Meinander, O., et al. (2014), Brief communication: Light-absorbing impurities can reduce the density of melting snow, *Cryosphere*, *8*(3), 991–995, doi:10.5194/tc-8-991-2014.

Mie, G. (1908), Beiträge zur Optik trüber Medien, speziell kolloidaler Metallösungen, *Ann. Phys.*, *330*(3), 377–445, doi:10.1002/andp.19083300302.
Myhre, G., et al. (2013), 2013: Anthropogenic and Natural Radiative Forcing, in *Climate Change 2013: The Physical Science Basis. Contribution of Working Group I to the Fifth Assessment Report of the Intergovernmental Panel on Climate Change*, pp. 659–740, Cambridge Univ. Press, Cambridge, U. K.
Oerlemans, J., R. H. Giesen, and M. R. Van Den Broeke (2009), Retreating alpine glaciers: increased melt rates due to accumulation of dust (Vadret da Morteratsch, Switzerland), *J. Glaciol.*, *55*(192), 729–736, doi:10.3189/002214309789470969.
Painter, T. H., and J. Dozier (2004), Measurements of the hemispherical-directional reflectance of snow at fine spectral and angular resolution, *J. Geophys. Res.*, *109*, D18115, doi:10.1029/2003JD004458.
Painter, T. H., A. P. Barrett, C. C. Landry, J. C. Neff, M. P. Cassidy, C. R. Lawrence, K. E. McBride, and G. L. Farmer (2007), Impact of disturbed desert soils on duration of mountain snow cover, *Geophys. Res. Lett.*, *34*, L12502, doi:10.1029/2007GL030284.
Painter, T. H., J. S. Deems, J. Belnap, A. F. Hamlet, C. C. Landry, and B. Udall (2010), Response of Colorado River runoff to dust radiative forcing in snow, *Proc. Natl. Acad. Sci. U. S. A.*, *107*(40), 17,125–17,130, doi:10.1073/pnas.0913139107.
Painter, T. H., S. M. Skiles, J. S. Deems, A. C. Bryant, and C. C. Landry (2012a), Dust radiative forcing in snow of the upper Colorado river basin: 1. A 6 year record of energy balance, radiation, and dust concentrations, *Water Resour. Res.*, *48*, W07521, doi:10.1029/2012WR011985.
Painter, T. H., A. C. Bryant, and S. M. Skiles (2012b), Radiative forcing by light absorbing impurities in snow from MODIS surface reflectance data, *Geophys. Res. Lett.*, *39*, L17502, doi:10.1029/2012GL052457.
Painter, T. H., M. G. Flanner, G. Kaser, B. Marzeion, R. A. VanCuren, and W. Abdalati (2013a), End of the Little Ice Age in the Alps forced by industrial black carbon, *Proc. Natl. Acad. Sci. U.S.A.*, *110*(38), 15,216–15,221, doi:10.1073/pnas.1302570110.
Painter, T. H., F. C. Seidel, A. C. Bryant, S. McKenzie Skiles, and K. Rittger (2013b), Imaging spectroscopy of albedo and radiative forcing by light-absorbing impurities in mountain snow, *J. Geophys. Res. Atmos.*, *118*, 9511–9523, doi:10.1002/jgrd.50520.
Pedersen, C. A., J.-C. Gallet, J. Ström, S. Gerland, S. R. Hudson, S. Forsström, E. Isaksson, and T. K. Berntsen (2015), In situ observations of black carbon in snow and the corresponding spectral surface albedo reduction, *J. Geophys. Res. Atmos.*, *120*, 1476–1489, doi:10.1002/2014JD022407.
Pey, J., X. Querol, A. Alastuey, F. Forastiere, and M. Stafoggia (2013), African dust outbreaks over the Mediterranean Basin during 2001–2011: PM_{10} concentrations, phenomenology and trends, and its relation with synoptic and mesoscale meteorology, *Atmos. Chem. Phys.*, *13*(3), 1395–1410, doi:10.5194/acp-13-1395-2013.
Pope, A., and G. Rees (2014), Using in situ spectra to explore Landsat classification of glacier surfaces, *Int. J. Appl. Earth Obs. Geoinf.*, *27*, 42–52, doi:10.1016/j.jag.2013.08.007.
Prospero, J. M. (2002), Environmental characterization of global sources of atmospheric soil dust identified with the NIMBUS 7 Total Ozone Mapping Spectrometer (TOMS) absorbing aerosol product, *Rev. Geophys.*, *40*(1), 1002, doi:10.1029/2000RG000095.
Reynolds, R. L., et al. (2013), Composition of dust deposited to snow cover in the Wasatch Range (Utah, USA): Controls on radiative properties of snow cover and comparison to some dust-source sediments, *Aeolian Res.*, doi:10.1016/j.aeolia.2013.08.001.
Rhoades, C., K. Elder, and E. Greene (2010), The influence of an extensive dust event on snow chemistry in the Southern Rocky Mountains, *Arct. Antarct. Alp. Res.*, *42*(1), 98–105, doi:10.1657/1938-4246-42.1.98.
Richter, R. (2007), Atmospheric/topographic correction for satellite imagery (ATCOR - 2/3 User Guide), *ATCOR-2/3 User Guid. Version 6.3*, (February).
Ruth, U., et al. (2008), Proxies and measurement techniques for mineral dust in Antarctic ice cores, *Environ. Sci. Technol.*, *42*(15), 5675–5681, doi:10.1021/es703078z.
Ryan, J. C., A. L. Hubbard, J. E. Box, J. Todd, P. Christoffersen, J. R. Carr, T. O. Holt, and N. Snooke (2015), UAV photogrammetry and structure from motion to assess calving dynamics at Store Glacier, a large outlet draining the Greenland ice sheet, *Cryosphere*, *9*(1), 1–11, doi:10.5194/tc-9-1-2015.
Schaepman-Strub, G., M. E. Schaepman, T. H. Painter, S. Dangel, and J. V. Martonchik (2006), Reflectance quantities in optical remote sensing: Definitions and case studies, *Remote Sens. Environ.*, *103*(1), 27–42, doi:10.1016/j.rse.2006.03.002.
Sodemann, H., A. S. Palmer, C. Schwierz, M. Schwikowski, and H. Wernli (2006), The transport history of two Saharan dust events archived in an Alpine ice core, *Atmos. Chem. Phys.*, *6*(3), 667–688, doi:10.5194/acp-6-667-2006.
Steltzer, H., C. Landry, T. H. Painter, J. Anderson, and E. Ayres (2009), Biological consequences of earlier snowmelt from desert dust deposition in alpine landscapes, *Proc. Natl. Acad. Sci. U.S.A.*, *106*(28), 11,629–11,634, doi:10.1073/pnas.0900758106.
Sterle, K. M., J. R. McConnell, J. Dozier, R. Edwards, and M. G. Flanner (2013), Retention and radiative forcing of black carbon in eastern Sierra Nevada snow, *Cryosphere*, *7*(1), 365–374, doi:10.5194/tc-7-365-2013.
Thevenon, F., F. S. Anselmetti, S. M. Bernasconi, and M. Schwikowski (2009), Mineral dust and elemental black carbon records from an Alpine ice core (Colle Gnifetti glacier) over the last millennium, *J. Geophys. Res.*, *114*, D17102, doi:10.1029/2008JD011490.
Tschiersch, J., B. Hietel, P. Schramel, and F. Trautner (1990), Saharan dust at jungfraujoch, *J. Aerosol Sci.*, *21*, S357–S360, doi:10.1016/0021-8502(90)90256-W.
Warren, S. G. (1982), Optical properties of snow, *Rev. Geophys.*, *20*(1), 67, doi:10.1029/RG020i001p00067.
Warren, S. G. (2013), Can black carbon in snow be detected by remote sensing?, *J. Geophys. Res. Atmos.*, *118*, 779–786, doi:10.1029/2012JD018476.
Warren, S. G., and W. J. Wiscombe (1980), A model for the spectral albedo of snow. II: Snow containing atmospheric aerosols, *J. Atmos. Sci.*, *37*, 2734–2745, doi:10.1175/1520-0469(1980)037<2734:AMFTSA>2.0.CO;2.
Westoby, M. J., J. Brasington, N. F. Glasser, M. J. Hambrey, and J. M. Reynolds (2012), "Structure-from-Motion" photogrammetry: A low-cost, effective tool for geoscience applications, *Geomorphology*, *179*, 300–314, doi:10.1016/j.geomorph.2012.08.021.
Whitehead, K., B. J. Moorman, and C. H. Hugenholtz (2013), Brief Communication: Low-cost, on-demand aerial photogrammetry for glaciological measurement, *Cryosphere*, *7*(6), 1879–1884, doi:10.5194/tc-7-1879-2013.
Wientjes, I. G. M., R. S. W. Van de Wal, G. J. Reichart, A. Sluijs, and J. Oerlemans (2011), Dust from the dark region in the western ablation zone of the Greenland ice sheet, *Cryosphere*, *5*(3), 589–601, doi:10.5194/tc-5-589-2011.
Winton, V. H. L., G. B. Dunbar, N. A. N. Bertler, M.-A. Millet, B. Delmonte, C. B. Atkins, J. M. Chewings, and P. Andersson (2014), The contribution of aeolian sand and dust to iron fertilization of phytoplankton blooms in southwestern Ross Sea, Antarctica, *Global Biogeochem. Cycles*, *28*, 423–436, doi:10.1002/2013GB004574.
Wiscombe, W. J. (1980), Improved Mie scattering algorithms, *Appl. Opt.*, *19*(*9*), 1505–1509, doi:10.1364/AO.19.001505.
Wiscombe, W. J., and S. G. Warren (1980), A model for the spectral albedo of snow. I: Pure snow, *J. Atmos. Sci.*, *37*(12), 2712–2733, doi:10.1175/1520-0469(1980)037<2712:AMFTSA>2.0.CO;2.
Yasunari, T. J., R. D. Koster, K.-M. Lau, T. Aoki, Y. C. Sud, T. Yamazaki, H. Motoyoshi, and Y. Kodama (2011), Influence of dust and black carbon on the snow albedo in the NASA Goddard Earth Observing System version 5 land surface model, *J. Geophys. Res.*, *116*, D02210, doi:10.1029/2010JD014861.
Yasunari, T. J., R. D. Koster, K.-M. Lau, and K.-M. Kim (2015), Impact of snow darkening via dust, black carbon, and organic carbon on boreal spring climate in the Earth system, *J. Geophys. Res. Atmos.*, *120*, doi:10.1002/2014JD022977.